Materials Advances

Check for updates

Crystal structure, luminescence properties and application performance of color tuning Y2Mg2Al2Si2O12:Ce3+,Mn2+ phosphors for warm white light-emitting diodes

Xiangting Zhang,[a] Dan Zhang,[a] Dongxiao Kan,[b] Tong Wu,[a] Yanhua Song, [ID] *[a] Keyan Zheng,[a] Ye Sheng, [ID] [a] Zhan Shi [ID] [c] and Haifeng Zou*[a]

Warm white light-emitting diodes (WLEDs) with low correlated color temperature (CCT < 5000 K) have a wide range of applications in solid-state lighting. This work reports $Y_2Mg_2Al_2Si_2O_{12}$ (YMAS):Ce^{3+},Mn^{2+} phosphors for warm WLEDs, which are suitable for current mainstream blue LED chips (λ = 460 nm). The crystal structure and site occupation of the synthetic materials conforms to the design, and they are studied experimentally and computationally. The spectral red shift of YMAS:Ce^{3+},Mn^{2+} phosphors can reach up to 77 nm compared with the commercial YAG:Ce phosphor. Their comparatively excellent thermal stability and good chromaticity stability are proved. Theoretically, this series of phosphors, combined with blue chips, can achieve almost the whole area of warm white light emission. Their practical application performance in LEDs is demonstrated, and the CCT of the LEDs achieves an effective optimization (∼4000 K). The simple synthetic method, effective color point tuning and good stability make YMAS:Ce^{3+},Mn^{2+} an attractive candidate phosphor for warm white LED lighting.

1. Introduction

White light-emitting diodes (WLEDs) have become the new generation of solid-state lighting source, with their high efficiency, good stability, long working life, environmental friendliness, *etc.*[1–3] Therein, phosphor-converted WLEDs (pc-WLEDs) are the mainstream applications. Currently, commercial pc-WLEDs involve the combination of blue chips (GaN/InGaN) with the $Y_3Al_5O_{12}$:Ce^{3+} (YAG:Ce) yellow phosphor.[4] However, due to their lack of red components, it is difficult to achieve a warm white light with a correlated color temperature (CCT) below 5000 K. According to some reports, high CCT can affect human health, especially that of human eyes.[5,6] In addition, the CCT has a significant impact on people's mood. Warmer lighting demonstrates a more positive, less negative effect on people.[7] So, cold WLED lighting is not suitable for many lighting situations, such as homes, libraries, offices, hospitals, *etc.* At present, there are two main solutions to this problem. One is the introduction of additional red phosphors, while another is optimization of the single-matrix phosphor.[8–10] However, the first solution, namely combination of the blue chip with yellow and red phosphors, is not the best option because of certain problems. First, the different stabilities of the two phosphors results in unstable emission of whole white light. Second, at present, commercial red phosphors have poor stability (K_2SiF_6:Mn^{4+}) or harsh synthesis conditions (CaAlSiN$_3$:Eu^{2+} and $Sr_2Si_5N_8$:Eu^{2+}) or cause serious environmental pollution (Y_2O_2S:Eu^{3+}).[11,12] Therefore, it is of great practical significance to develop phosphors that can be used in LED chips to achieve warm white light emission with low CCT.

Against this background, regulation of the spectra for the YAG:Ce system has been widely studied by researchers. Such work is mainly concentrated on two methods. One is modification of the host structure, including cationic or anionic substitution. For instance, Chen *et al.* reported the $Tb_3Al_5O_{12}$:Ce^{3+} phosphor prepared by the sol-combustion method, and the sample showed a green-yellow emission centered at about 545–555 nm.[13] Ji *et al.* reported the $Y_2BaAl_4SiO_{12}$:Ce^{3+} phosphor, with a bright yellow emission with a peak at 537 nm.[14] Shang *et al.* researched the influence of Mg^{2+}–Si^{4+}/Ge^{4+} incorporation into YAG, and the emission spectra could be regulated from 528 to 569 nm.[15] Another method is to introduce co-activated ions, which exhibit red emission. Jang *et al.* reported the YAG:Ce^{3+},Pr^{3+} phosphor, in which a sharp peak at around 610 nm is introduced.[16] Sun *et al.* reported the YAG:Ce^{3+},Sm^{3+}

[a] College of Chemistry, Jilin University, Qianjin Street 2699, Changchun 130012, China. E-mail: yhsong@jlu.edu.cn, zouhf@jlu.edu.cn

[b] College of Physics, Jilin University, Qianjin Street 2699, Changchun 130012, China

[c] State Key Laboratory of Inorganic Synthesis and Preparative Chemistry, College of Chemistry, Jilin University, Qianjin Street 2699, Changchun 130012, China

phosphor, in which the emission spectra showed a gradual red shift from 525 to 540 nm with increase in Sm^{3+} concentration, and the peak for Sm^{3+} also appeared at 617 nm.[17] Jia *et al.* reported the incorporation of Mn^{2+}–Si^{4+} in YAG:Ce, with the obtained phosphor exhibiting Ce^{3+} emission at 540 nm and Mn^{2+} emission at 594 nm.[11] These reports indicate that both strategies are feasible. However, their practical application performance still needs to be further improved.

In our previous work, the $Y_2Mg_2Al_2Si_2O_{12}$ (YMAS) host was designed, synthesized and studied.[18,19] It can be considered as a substitution of Y^{3+}/Al^{3+}–Al^{3+} by Mg^{2+}–Si^{4+} in YAG. As a modified derivative material of the YAG garnet structure, this leads to changes in photoluminescence properties. Meanwhile, the introduced Mg^{2+} sites are very suitable for the further introduction of Mn^{2+} ion, which leads to unexpected luminescence and potential applications. Thus, in this work, strategies for regulation of the matrix structure and the introduction of co-activated ions are simultaneously applied to optimize the fluorescence spectra and improve the application performance. The crystal structure, site occupation, luminescence properties, thermal stability, chromaticity stability and application performance are discussed in detail. The results show that the simple synthetic method, effective color point tuning and good stability make YMAS:xCe^{3+},yMn^{2+} an attractive candidate phosphor for warm white LED lighting.

2. Experimental and computational

2.1 Synthesis

The samples of YMAS:xCe^{3+},yMn^{2+} were synthesized by the solid-state reaction method. The raw materials were Y_2O_3, MgO, Al_2O_3, SiO_2, $Ce_2(CO_3)_3$ and $MnCO_3$. The purity of the rare earth oxides or carbonates was 99.99%, and the other raw materials were of analytical reagent grade. The quantities were weighed by stoichiometric ratio. All raw materials were homogeneously mixed and ground with a certain amount of ethanol for 30 min. The mixture was then calcined in a reducing atmosphere (10% H_2/90% N_2) at 1400 °C for 6 h. The final samples were obtained after cooling and grinding thoroughly.[18]

2.2 LED fabrication

LEDs were fabricated with the YMAS:xCe^{3+},yMn^{2+} phosphors and blue chips (λ = 460 nm). The phosphors were well mixed with epoxy resin glue and hardening agent, with a mass ratio of 4 : 1 : 4. Then, the phosphor-epoxy resin-hardening agent mixture was coated onto the LED chip. Finally, the encapsulated LED devices were cured at 120 °C for 2 h.[19]

2.3 Characterization

The X-ray diffraction (XRD) patterns of YMAS:xCe^{3+},yMn^{2+} samples were collected by a Panalytical BV Empyrean diffractometer operating at 40 kV and 40 mA. The X-ray photoelectron spectroscopy (XPS) spectra were measured by a Thermo Fisher Scientific Escalab-250. The Rietveld refinement was performed using the GSAS program.[20] Morphological characterization was

investigated by scanning electron microscopy (SEM, Hitachi, SU8020) and energy-dispersive spectroscopy (EDS, Bruker) elemental mapping technique. The spectroscopic data, including photoluminescence excitation (PLE) spectra, photoluminescence (PL) spectra, fluorescence decay curves and temperature-dependent PL spectra were recorded by a Horiba Jobin Yvon Fluoro Max-4 equipped with relevant accessories. The electroluminescent (EL) spectra and relevant parameters for the LEDs were measured by an Everfine HAAS-1200 test system.

2.4 Computational details

First-principles computations based on density functional theory (DFT) were carried out by the plane-wave technique, as implemented in the Vienna ab initio simulation package (VASP) code.[21] The YMAS:Mn^{2+} crystals were modeled as $1 \times 1 \times 1$ supercells containing 160 atoms, in which one of 16 Mg^{2+} was substituted by a Mn^{2+}, where, Mn replaced the Mg(1) site as eight-coordinate in Model-1 and Mn occupied the Mg(2) site as six-coordinate in Model-2. The exchange-functional energy was described with the Perdew–Burke–Ernzerhof generalized gradient approximation (GGA-PBE)[22] using the plane-wave basis set with an energy cut-off of 500 eV. Within the constrained supercells, the model structures were fully optimized until the total energies and the forces on the atoms were converged to 10^{-5} eV and 0.01 eV Å^{-1}, respectively. The Brillouin zone was sampled with a $7 \times 7 \times 7$ uniform k-point mesh.[19]

3. Results and discussion

3.1 Crystal structure and site occupation

The XRD patterns of the as-prepared YMAS:xCe^{3+} and YMAS:0.06Ce^{3+},yMn^{2+} samples are shown in Fig. 1a and b. All the diffraction peaks can be indexed to the standard card of YAG (PDF #88-2048), which reveals that these samples have a single crystal phase. The peak at 2θ = 33.4 can be properly assigned to the (420) plane, which is the dominant plane of garnet crystal structure. Fig. 1c exhibits the XPS survey spectrum of YMAS:0.06Ce^{3+},0.25Mn^{2+} in the binding energy range of 0–1200 eV, which indicates the presence of Y, Mg, Al, Si, Ce, Mn and O. The corresponding high-revolution XPS spectrum for Mn^{2+} is shown in Fig. 1d. The Mn 2p presents two separate peaks located at 654.2 and 642.3 eV with an energy difference of 11.9 eV. These two peaks can be assigned to Mn 2p$_{1/2}$ and Mn 2p$_{3/2}$, respectively.[23] In addition, Pan *et al.* reported that the Mn^{2+} occupied the Mg^{2+} site with a coordination number of eight in the $MgY_2Al_4SiO_{12}$ host, in which the binding energy of the divalent cation Mn 2p$_{3/2}$ was 653.4 eV and the energy difference of Mn 2p was 11.5 eV. A bigger binding energy will be observed for the cations with a higher coordination number of O^{2-}.[24] As we reported earlier,[18] in the YMAS host, Y and Mg(1) occupy the dodecahedral sites with eight coordination, and Mg(2) and Al(1) occupy the octahedral sites with six coordination. Based on XPS results and the literature, and on account of the same valence state and approximate ionic radii ($R_{Y^{3+}}$ = 1.02 Å, $R_{Ce^{3+}}$ = 1.14 Å, $R_{Mg^{2+}}$ = 0.89 Å and $R_{Mn^{2+}}$ = 0.96 Å for
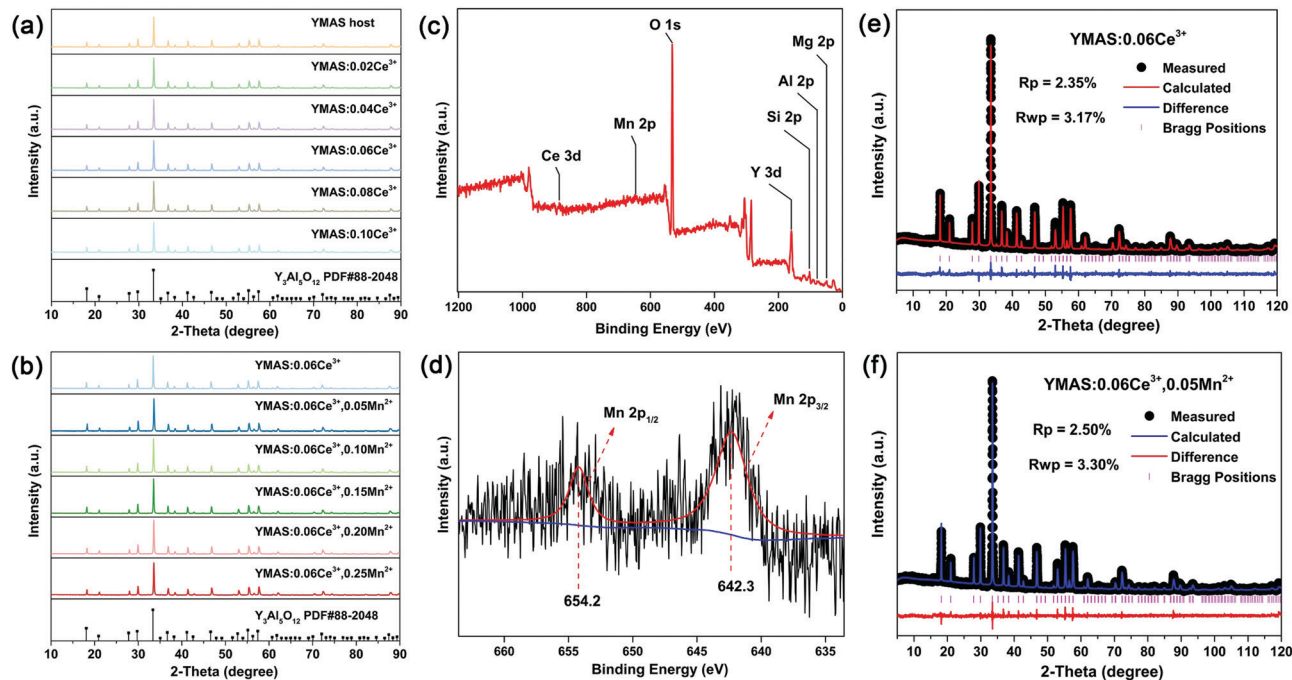
Fig. 1 XRD patterns of YMAS:xCe^{3+} (x = 0–0.10) (a) and YMAS:0.06Ce^{3+},yMn^{2+} (y = 0–0.25) (b) with the standard of Y$_3$Al$_5$O$_{12}$ (PDF #88-2048). The XPS survey spectrum (c) and high-revolution spectrum (d) of YMAS:0.06Ce^{3+},0.25Mn^{2+}. Rietveld refinement results of YMAS:0.06Ce^{3+} (e) and YMAS:0.06Ce^{3+},0.05Mn^{2+} (f).

CN = 8, $R_{Mg^{2+}}$ = 0.72 Å and $R_{Mn^{2+}}$ = 0.83 Å for CN = 6, where R stands for the ionic radius and CN is the coordination number), the Ce^{3+} ions prefer to occupy the dodecahedral sites of Y. The Mn^{2+} ions may prefer to occupy the dodecahedral sites of Mg(1) and the octahedral sites of Mg(1), respectively. According to this design, the XRD data of YMAS:0.06Ce^{3+} and YMAS:0.06-Ce^{3+},0.05Mn^{2+} were executed for the Rietveld refinement. As shown in Fig. 1e and f, the calculated patterns agree well with the experimental ones. The primary reliability factors in the structural refinement are converged to R_p = 2.35%, R_{wp} = 3.17% for YMAS:0.06Ce^{3+} and R_p = 2.50%, R_{wp} = 3.30% for YMAS:0.06-Ce^{3+},0.05Mn^{2+}, which demonstrates that the refined crystal structures are reasonably accepted. The Rietveld refinement results and crystallographic parameters of the YMAS host, YMAS:0.06Ce^{3+} and YMAS:0.06Ce^{3+},0.05Mn^{2+} are listed in Table 1. The variation of crystallographic parameters is consistent with the differences in the radii of the ions, further indicating the effective doping of Ce^{3+} and Mn^{2+} in the YMAS host. To further understand the site-selective occupation of

Mn^{2+} in the YMAS host, DFT calculations within the supercell model were carried out. As shown in Fig. 2, two different Mg-ion lattice sites were selected in the optimized YMAS model. Both Mg(1) and Mg(2) may be replaced by Mn ion. So, the models of Mn^{2+} substitution at different sites were created, calculated and compared. Therein, Mn occupied the Mg(1) site with eight coordination (Model-1) and occupied the Mg(2) site with six coordination (Model-2), respectively. The DFT total energies of Model-1 and Model-2 revealed that Mn^{2+} strongly preferred to be at the Mg(1) site over the Mg(2) site (by 1.14 eV).[25] In summary, it is proved that Mn^{2+} may have a preference for the dodecahedral sites with eight coordination in YMAS:Ce^{3+},Mn^{2+}. However, so far, there are few characterization methods to directly and clearly detect the chemical environment of Mn^{2+}. The site occupation of Mn^{2+} in YMAS remains to be further studied. The schematic diagrams of the crystal structure and activator occupancy are shown in Fig. 3.

Fig. 4 presents the morphology of the YMAS:0.06Ce^{3+},0.20Mn^{2+} sample. It is obvious that the crystal surface is relatively smooth and clean, which suggests that the material has excellent crystallinity. Moreover, the compositional uniformity of the sample was inspected with the EDS elemental mapping technique in SEM, as shown in Fig. 4b–h. Evidently, the Y, Mg, Al, Si, Ce, Mn and O elements in this material are very homogeneous.

3.2 Luminescence properties of YMAS:Ce^{3+}

Fig. 5a shows the PLE and PL spectra of YMAS:0.06Ce^{3+}. In the test range, the PLE band almost covers the entire spectral range of 300–550 nm. In particular, the broadband excitation from 375 to 550 nm with 450 nm as the dominant peak means that it
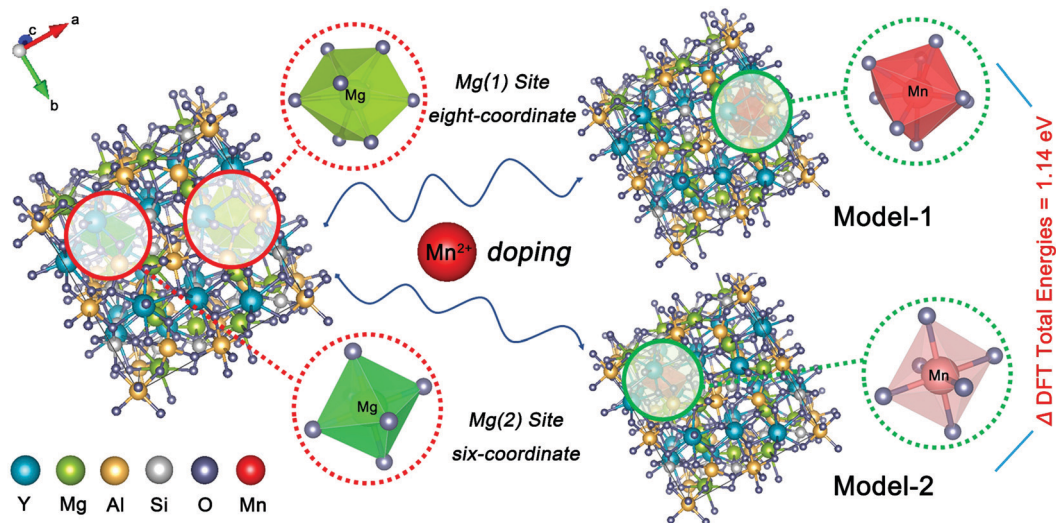
Table 1 Rietveld refinement results and crystallographic parameters of the YMAS host, YMAS:0.06Ce^{3+} and YMAS:0.06Ce^{3+},0.05Mn^{2+}

	Crystallographic parameters			Reliability factors	
Samples	$a = b = c$ (Å)	V (Å^3)	$\alpha = \beta = \gamma$ (deg)	R_p (%)	R_{wp} (%)
YMAS host	11.9774	1718.2551	90	2.22	2.92
YMAS:0.06Ce^{3+}	11.9778	1718.4361	90	2.35	3.17
YMAS:0.06Ce^{3+},0.05Mn^{2+}	11.9788	1718.8749	90	2.50	3.30

Fig. 2 The schematic diagrams of calculation models of Mn ion in YMAS with different occupying sites.
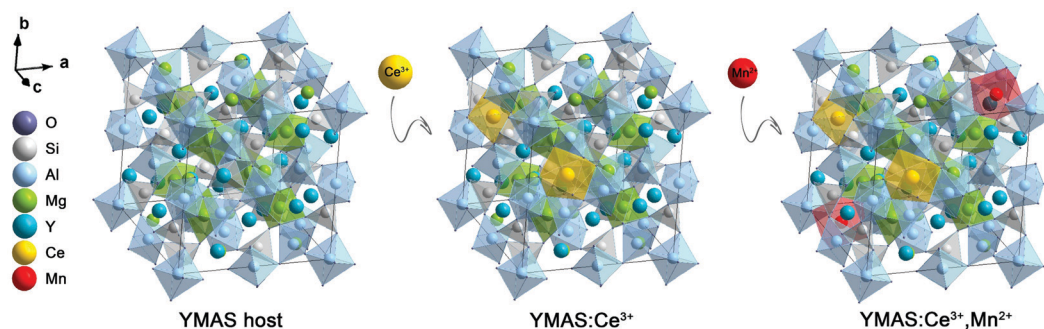
Fig. 3 Crystal structures of YMAS host, YMAS:Ce^{3+} and YMAS:Ce^{3+},Mn^{2+}.
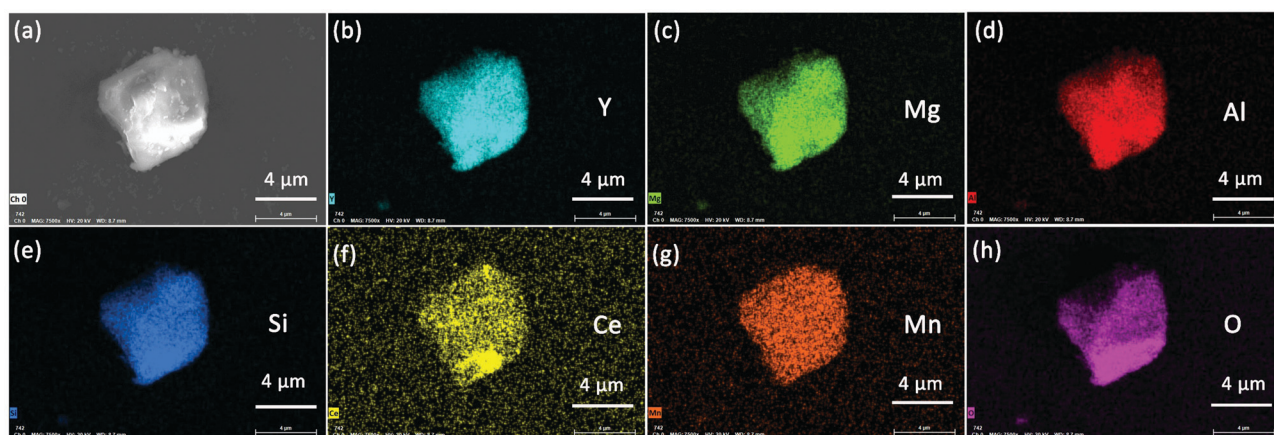

Fig. 4 SEM and element mapping images of YMAS:0.06Ce^{3+},0.20Mn^{2+}

can match well with the current mainstream blue chip. These two excitation bands are attributed to the electronic transitions of Ce^{3+} ions from the 4f ground state to the field-splitting levels of its 5d state. YMAS:0.06Ce^{3+} exhibits a yellow emission band with 564 nm as the center, which corresponds to the 5d → 4f transition of the Ce^{3+} ions. The PL spectra and normalized PL spectra of YMAS:$x$$Ce^{3+}$ (x = 0.01–0.10) excited at 450 nm are shown in Fig. 5b and c. With increase in Ce^{3+} doping concentration, the
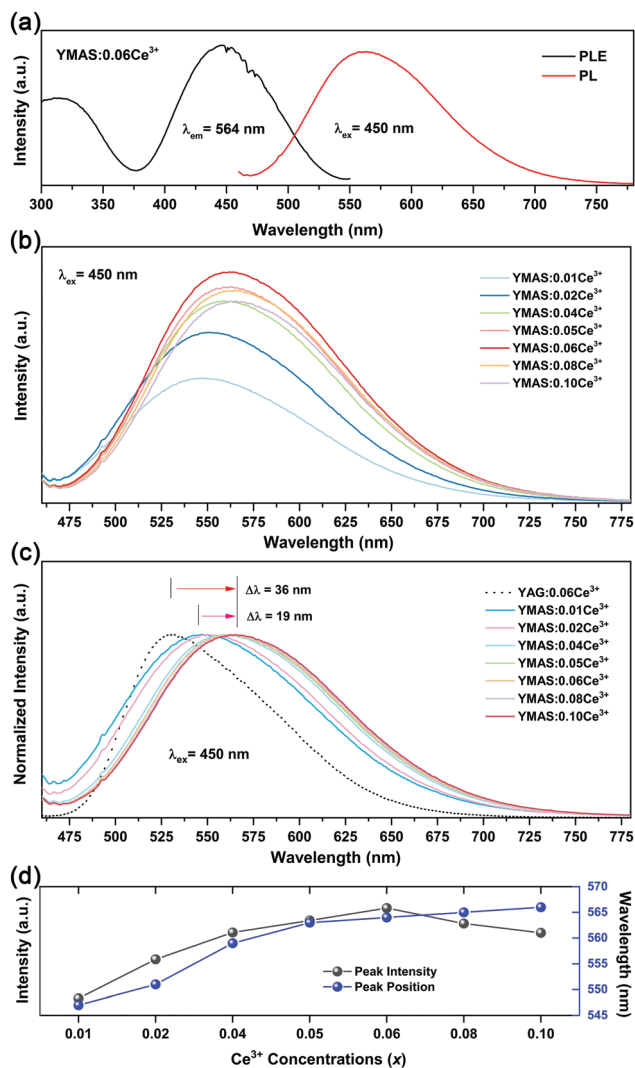
Fig. 5 (a) PLE (λ_{em} = 564 nm) and PL (λ_{ex} = 450 nm) spectra of YMAS:0.06Ce^{3+}. (b) PL spectra and (c) normalized PL spectra of YMAS:xCe^{3+} (x = 0.01–0.10) excited at 450 nm. (d) The variation of peak intensity and peak position with Ce^{3+} concentration.

PL spectra gradually red shift from 547 nm (x = 0.01) to 566 nm (x = 0.10). There are two probable causes of this spectral red shift. One is that the increase in doping concentration increases the degree of crystal field splitting, and so the emission shifts gradually.[26] Another reason is reabsorption. In Fig. 5a, there is obvious spectral overlap in the range 460–550 nm. As a consequence, with the increase in Ce^{3+} concentration, the probability of the emission band being absorbed in the short-wave side increases continuously. Subsequently, the absorption of spectral energy on the short-wave side is converted to the full width of the Ce^{3+} emission band, which leads to the spectral red shift.[27] In addition to spectral shift, emission intensity also varies with doping concentration. As shown in Fig. 5d, the PL intensity of YMAS:xCe^{3+} (x = 0.01–0.10) continuously increases with x, reaching a maximum at x = 0.06, and then decreases with further increase of x due to the concentration quenching effect.[28]

3.3 Luminescence properties of YMAS:Ce^{3+},Mn^{2+}

Compared with YAG:Ce phosphor, YMAS:xCe^{3+} realized spectral regulation of 36 nm. However, this is not enough for applications in LED lighting for warm white light emission. Mn^{2+} is a widely used red light activator in inorganic phosphors. So, Mn^{2+} was introduced into this system. The PLE and PL spectra of YMAS:0.10Mn^{2+} are shown in Fig. 6a. The luminescence center of Mn^{2+} ions is located at 606 nm in YMAS, which is attributed to the spin-forbidden $^4T_1 \rightarrow {}^6A_1$ transition. Fig. 6b shows the PL intensity comparison of YMAS:0.06Ce^{3+} and YMAS:0.10Mn^{2+} under optimal excitation conditions measured at room temperature. The PL intensity of Ce^{3+} is more than 20 times that of Mn^{2+} in the YMAS. Even though the luminescence of Mn^{2+} is very weak due to the forbidden transition, the luminous intensity can be effectively enhanced through the sensitizing effect of Ce^{3+}.[29,30] As shown in Fig. 7a–c, the PL spectra of YMAS:0.06Ce^{3+},yMn^{2+} samples exhibit a significant red shift with increase in Mn^{2+} doping concentration. When y = 0.25, the dominant peak of the emission spectrum is located at 606 nm, which achieves a red shift of 42 nm compared with YMAS:0.06Ce^{3+}. In particular, compared with the commercial YAG:Ce phosphor, the spectral red shift of YMAS:0.06Ce^{3+},0.25Mn^{2+} phosphor is up to 77 nm. As the luminescence of Mn^{2+} ion is almost entirely dependent on the energy transfer of the Ce^{3+} ion, the overall emission intensity of YMAS:0.06Ce^{3+},yMn^{2+} is gradually decreasing, along with the color tuning. Therefore, in practical applications, the balance between intensity sacrifice and color optimization should be considered. To investigate the cause of the spectral red shift, a series of YMAS:0.06Ce^{3+},zCa^{2+} (z = 0–0.20) samples were prepared. Both Ca^{2+} ($R_{Ca^{2+}}$ = 1.12 Å for CN = 8 and $R_{Ca^{2+}}$ = 1.00 Å for CN = 6) and Mn^{2+} ions have larger radii than Mg^{2+} ions, which will have a consistent effect on the crystal field.
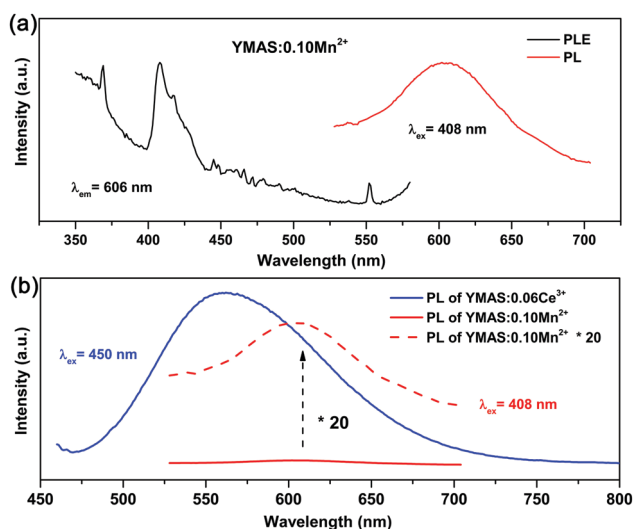

Fig. 6 (a) PLE (λ_{em} = 606 nm) and PL (λ_{ex} = 408 nm) spectra of YMAS:0.10Mn^{2+}. (b) The PL intensity comparison of YMAS:0.06Ce^{3+} and YMAS:0.10Mn^{2+} under optimal excitation conditions measured at room temperature.
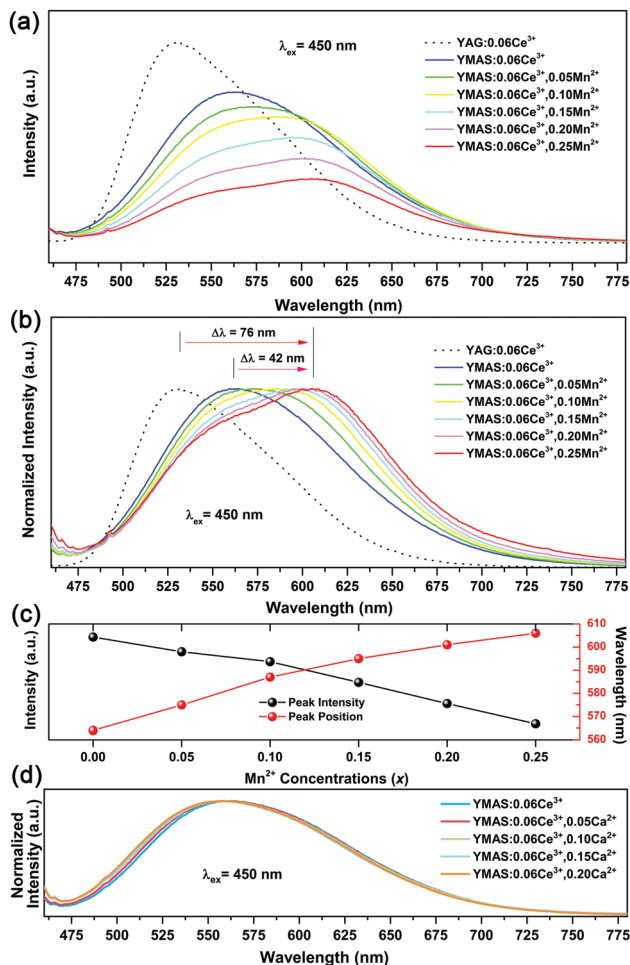
Fig. 7 (a) PL spectra and (b) normalized PL spectra of YMAS:0.06-Ce^{3+},yMn^{2+} (y = 0–0.25) excited at 450 nm. (c) The variation of peak intensity and peak position with Mn^{2+} concentration. (d) Normalized PL spectra of YMAS:0.06Ce^{3+},zCa^{2+} (z = 0–0.20) excited at 450 nm.

However, as shown in Fig. 7d, the spectra barely move, which preliminarily indicates that the primary cause of spectral red shift in YMAS:Ce^{3+},Mn^{2+} is energy transfer rather than the crystal field effect.

3.4 Energy transfer in YMAS:Ce^{3+},Mn^{2+}

The color tuning of YMAS:0.06Ce^{3+},yMn^{2+} is ascribed to the non-radiative energy transfer from Ce^{3+} to Mn^{2+} (ET$_{Ce^{3+}-Mn^{2+}}$). And, with increasing Mn^{2+} concentration, the fact that the PL spectra of YMAS:0.06Ce^{3+},yMn^{2+} are composed of two peaks becomes more and more obvious, as shown in Fig. 7a or b. For YMAS:0.06Ce^{3+},0.25Mn^{2+}, the broad emission band can be separated into two sub-Gaussian components. The peak of Ce^{3+} is at ~541 nm (18 475 cm^{-1}) and that of Mn^{2+} is at ~611 nm (16 369 cm^{-1}), as shown in Fig. 8a. The result of the Gaussian fitting is credible, taking the PL spectra of YMAS:xCe^{3+} and YMAS:Mn^{2+} as references. To further identity the evidence of ET$_{Ce^{3+}-Mn^{2+}}$, the decay curves of the Ce^{3+} ions in YMAS:0.06-Ce^{3+},yMn^{2+} were measured under excitation at 450 nm and monitored at 564 nm, as shown in Fig. 8b. The decay curves
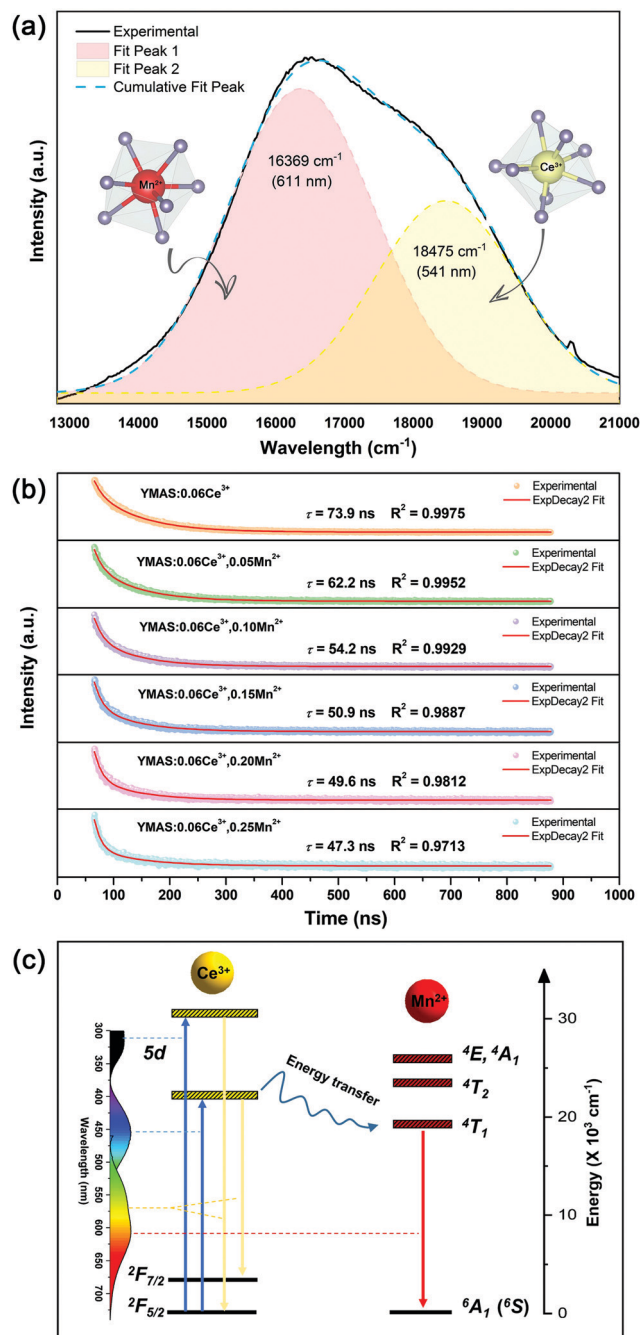

Fig. 8 (a) Gaussian fitting results of PL bands for YMAS:0.06Ce^{3+},0.25Mn^{2+}. (b) Decay curves and lifetime values for YMAS:0.06Ce^{3+},yMn^{2+} (y = 0–0.25) excited at 450 nm and monitored at 564 nm. (c) Schematic diagram of energy transfer in Ce^{3+}-Mn^{2+} co-doped YMAS phosphor.

were well fitted with a second-order exponential equation as follows:[31,32]

$$I = A_1 \exp(-t/\tau_1) + A_2 \exp(-t/\tau_2) \tag{1}$$

where I is the luminous intensity, A_1 and A_2 are exponential constants, t is the time and τ_1 and τ_2 are rapid and slow decay constants for the exponential component. The average decay time (τ) can be calculated with the following equation:[33,34]

$$\tau = (A_1\tau_1{}^2 + A_2\tau_2{}^2)/(A_1\tau_1 + A_2\tau_2) \qquad (2)$$

Then, the values of the average decay times were determined to be 73.9, 62.2, 54.2, 50.9, 49.6 and 47.3 ns for YMAS:0.06-Ce^{3+},$y$$Mn^{2+}$ with y = 0, 0.05, 0.10, 0.15, 0.20 and 0.25, respectively. This suggests that a fluorescence decay process takes place quickly in the YMAS:0.06Ce^{3+},$y$$Mn^{2+}$ system, which is the strong evidence for the energy transfer $ET_{Ce^{3+}-Mn^{2+}}$. In the case of energy transfer, the fluorescence lifetimes of the sensitizers are shortened because of the additional decay channels, which shortens the lifetimes of the excited state.[35] Moreover, the $ET_{Ce^{3+}-Mn^{2+}}$ efficiency (η) can be obtained by using the equation:[36,37]

$$\eta = 1 - \tau_s/\tau_{s0} \qquad (3)$$

where τ_s and τ_{s0} are the lifetimes of Ce^{3+} in the absence and presence of Mn^{2+}, respectively. The $ET_{Ce^{3+}-Mn^{2+}}$ efficiency gradually increases with increasing Mn^{2+} concentration, reaching $\sim$36% when y = 0.25. Based on the discussion above, the $ET_{Ce^{3+}-Mn^{2+}}$ mechanism in the YMAS host can be illustrated as shown in Fig. 8c. Upon blue light excitation, electrons of Ce^{3+} are excited to the 5d state, then the excited electrons return to the ground states ($^2F_{7/2}$ and $^2F_{5/2}$) in the form of radiative transitions. As a result, the phosphors emit yellow light. Due to the lowest 5d energy level of Ce^{3+} being slightly higher than the $^4T_1$ of Mn^{2+}, the energy transfer process happens easily from Ce^{3+} to the adjoining Mn^{2+} *via* non-radiation transition. Then, the $^4T_1 \rightarrow {}^6A_1$ transition of Mn^{2+} results in an orange-red emission.[38,39]

3.5 CIE of YMAS:Ce^{3+} and YMAS:Ce^{3+},Mn^{2+}

The color points of YMAS:$x$$Ce^{3+}$ (x = 0.01, 0.02, 0.04 and 0.06) and YMAS:0.06Ce^{3+},$y$$Mn^{2+}$ (y = 0.05, 0.10, 0.15 and 0.20) phosphors are plotted in Fig. 9. Therein, point B is the CIE coordinate of commercial blue chip (0.133, 0.064), point 0 is the commercial YAG:Ce yellow phosphor (0.433, 0.538), and point W is the standard white light point (0.333, 0.333). Obviously, current commercial LEDs fabricated by combining blue chip with YAG:Ce phosphor can only emit cold white light. The color point of YMAS:$x$$Ce^{3+}$,$y$$Mn^{2+}$ phosphors can be tuned from yellow (0.464, 0.493) to orange (0.541, 0.441). As a result, theoretically, this series of phosphors combined with the 460 nm chip can achieve almost the whole area of warm white light emission, which will greatly improve the quality of LED lighting applied to low CCT lighting scenes.

3.6 Application performance of phosphors and LEDs

In practical applications, temperature is a key factor affecting luminescence performance. Therefore, it is very important to evaluate the thermal stability and chromaticity stability of YMAS:$x$$Ce^{3+}$,$y$$Mn^{2+}$ phosphors. The temperature-dependent PL spectra and 2D mapping of YMAS:0.06Ce^{3+} and YMAS:0.06-Ce^{3+},0.05Mn^{2+} are shown in Fig. 10a–d. It is obvious that the emission intensity decreases with increase in temperature, no matter whether YMAS:0.06Ce^{3+} or YMAS:0.06Ce^{3+},0.05Mn^{2+} is used. The PL intensity of YMAS:0.06Ce^{3+} retained 94.4% at
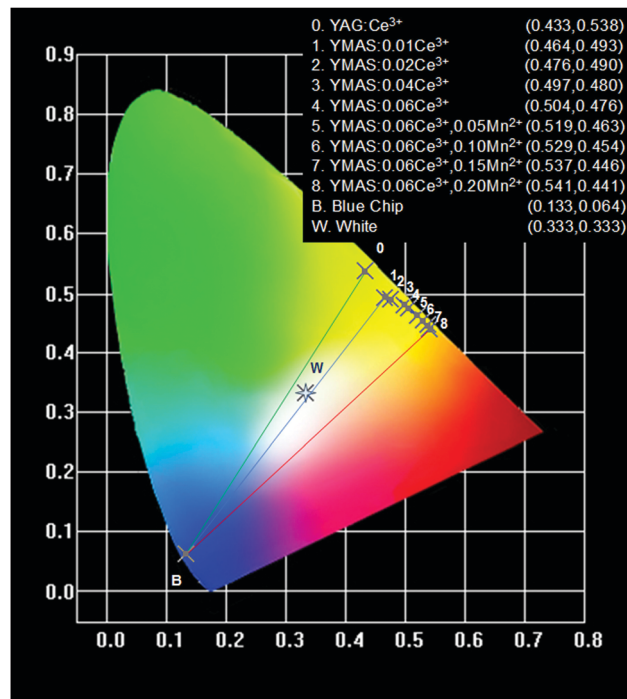

Fig. 9 CIE chromaticity coordinates of YAG:Ce^{3+}, YMAS:xCe^{3+} (x = 0.01, 0.02, 0.04 and 0.06) and YMAS:0.06Ce^{3+},yMn^{2+} (y = 0.05, 0.10, 0.15 and 0.20).

373 K and 87.8% at 423 K compared with the intensity measured at 298 K. For YMAS:0.06Ce^{3+},0.05Mn^{2+}, the corresponding values are 93.4% and 86.7%, at 373 K and 423 K, respectively. In addition, the shapes of the spectra remain almost constant with temperature in YMAS:0.06Ce^{3+}. For YMAS:0.06Ce^{3+},0.05Mn^{2+}, with increase of temperature, the emission bands appear to be blue shifted to some extent. This is mainly due to the fact that the emission reduction rate of Mn^{2+} is higher than that of Ce^{3+} as the temperature goes up. And the decrease in Mn^{2+} intensity is due to its transitions from lower to higher energy levels in the excited states, assisted by thermal active phonons.[12] The above results indicate that the YMAS:$x$$Ce^{3+}$,$y$$Mn^{2+}$ phosphors have comparatively excellent thermal stability. The change of CIE chromaticity coordinates of YMAS:0.06Ce^{3+} and YMAS:0.06Ce^{3+},0.05Mn^{2+} with increasing temperature are drawn in Fig. 10e and f. The CIE coordinates of YMAS:0.06Ce^{3+} shift to short wavelength from (0.507, 0.469) to (0.504, 0.471) to (0.501, 0.473) when the temperature changes from 298 K to 373 K to 423 K. For YMAS:0.06Ce^{3+},0.05Mn^{2+}, the coordinates are (0.518, 0.459) to (0.513, 0.462) to (0.508, 0.466), respectively. Compared to other reports,[12,40,41] these results indicate that the YMAS:$x$$Ce^{3+}$,$y$$Mn^{2+}$ phosphors have a good chromaticity stability.

The simple synthetic method, effective color point tuning and good stability make YMAS:$x$$Ce^{3+}$,$y$$Mn^{2+}$ an attractive candidate phosphor for warm white LED lighting. To demonstrate its potential application, a series of white LEDs were encapsulated by using the YMAS:$x$$Ce^{3+}$,$y$$Mn^{2+}$ phosphors and blue chips (λ = 460 nm). The photographs, electroluminescent spectra, relevant parameters and CIE chromaticity diagram of the devices
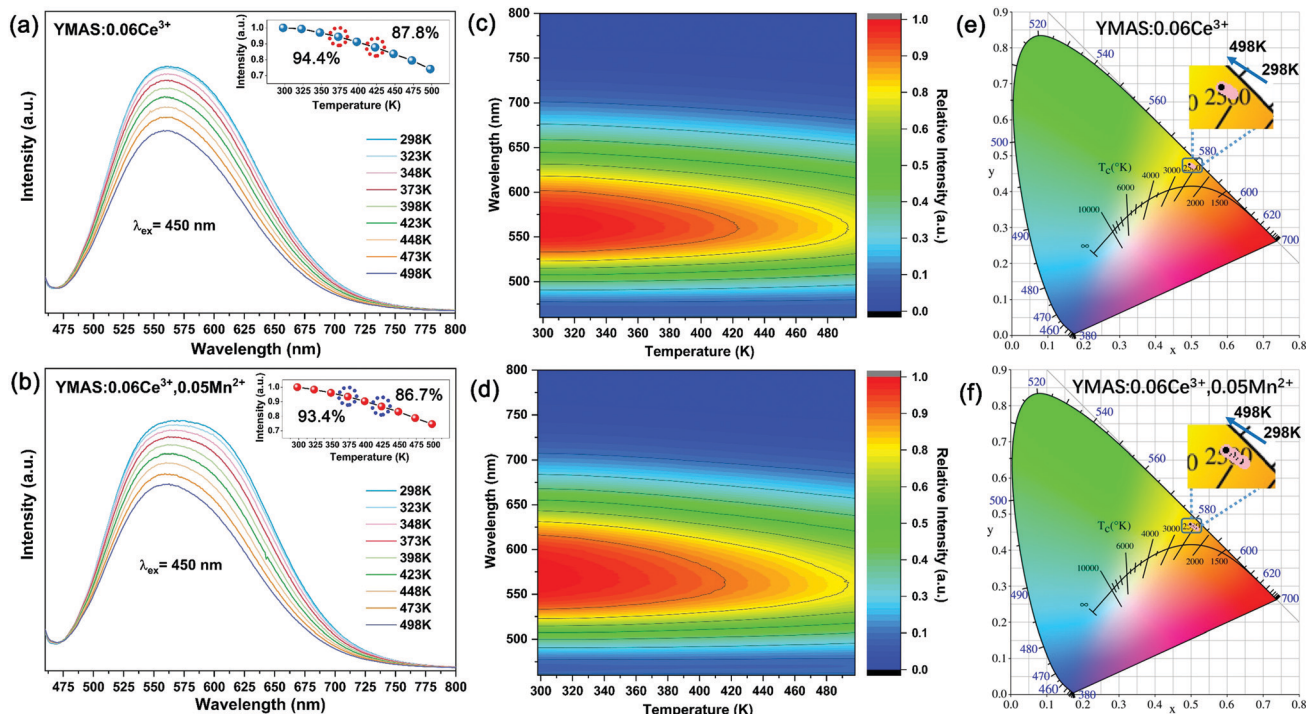
Fig. 10 Temperature-dependent PL spectra (λ_{ex} = 450 nm) of YMAS:0.06Ce^{3+} (a) and YMAS:0.06Ce^{3+},0.05Mn^{2+} (b); inset shows the variation of peak intensity with temperature. Two-dimensional (2D) mapping of PL spectra dependence on temperature for YMAS:0.06Ce^{3+} (c) and YMAS:0.06-Ce^{3+},0.05Mn^{2+} (d). CIE chromaticity coordinates of YMAS:0.06Ce^{3+} (e) and YMAS:0.06Ce^{3+},0.05Mn^{2+} (f) under various temperatures.

under a current of 20 mA are shown in Fig. 11. Compared with commercial LED lighting (LED-1) with cold white light emission at high CCT (CCT = 8976 K), the LED devices (LED-2–5) prepared by YMAS:xCe^{3+},yMn^{2+} samples can realize warm white light
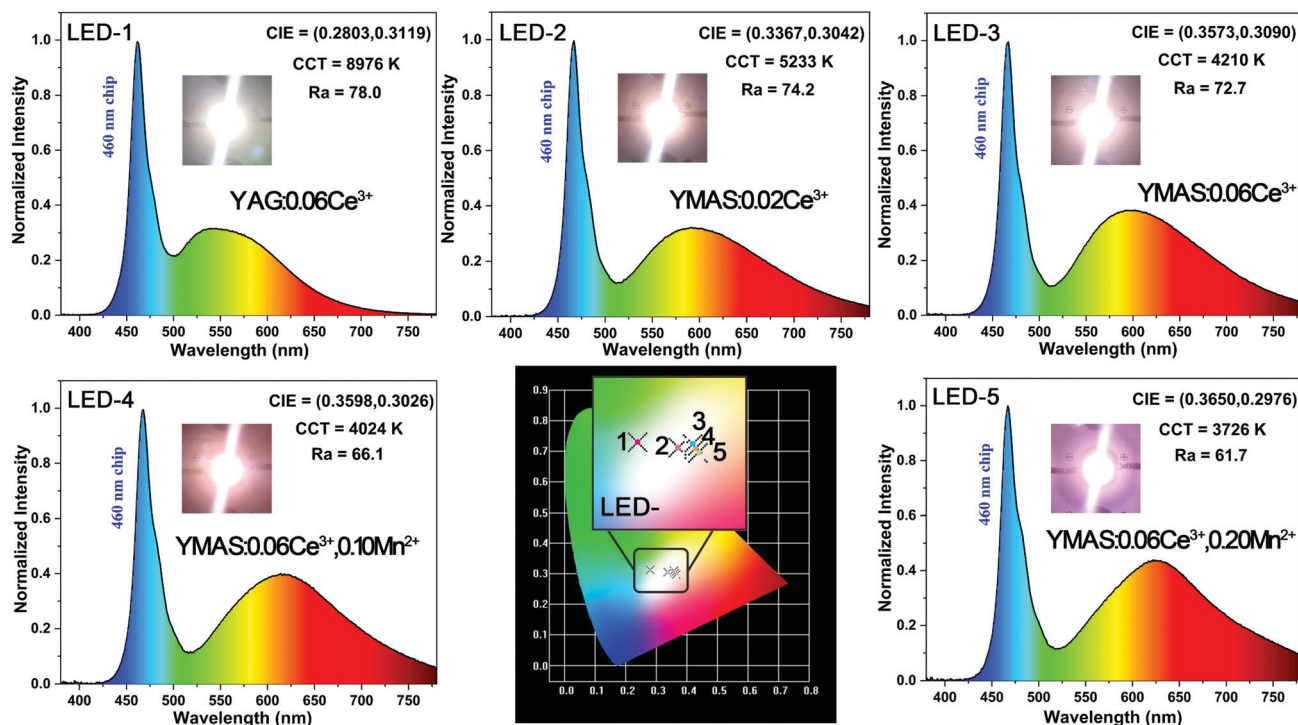

Fig. 11 Photographs, electroluminescence spectra, relevant parameters, CIE chromaticity diagram and performance of the LED devices driven by a 20 mA current.

emission at low CCT. By adjusting the doping level of the single activator and the energy transfer of double activators, the CCT of the LEDs achieves effective optimization (to $\sim$4000 K). In addition, the performance of the above LEDs can be further improved by optimizing the preparation process. Warm white light can create a warm, soft, comfortable atmosphere, which is suitable for homes, libraries, offices, hospitals, restaurants and many other indoor environments.

4. Conclusions

In summary, we have developed a series of yellow-orange YMAS:xCe^{3+},yMn^{2+} phosphors for warm WLEDs. The YMAS host is very suitable for the introduction of Ce^{3+} and Mn^{2+} due to the presence of multiple valence states and abundant cationic sites in the crystal lattices. The crystal structure of the materials was studied by XRD, XPS, Rietveld refinement, SEM and DFT calculations. The Mn^{2+} ions tend to occupy the Mg sites in the YMAS. Through adjusting the doping level, the YMAS:xCe^{3+} (x = 0.01–0.10) phosphors can realize the regulation of the luminescence center from 547 to 566 nm. Further, by introducing the Mn^{2+} activator and adjusting the energy transfer, YMAS:xCe^{3+},yMn^{2+} (y = 0.05–0.25) phosphors achieve a spectral red shift from 564 to 606 nm. Compared with commercial YAG:Ce phosphor, the spectral red shift of YMAS:xCe^{3+},yMn^{2+} phosphors can reach up to 77 nm. Theoretically, this series of phosphors combined with blue chip can achieve almost the whole area of warm white light emission. In addition, the YMAS:xCe^{3+},yMn^{2+} phosphors have comparatively excellent thermal stability and good chromaticity stability, which meet the requirements of LED lighting applications. Compared with commercial LEDs with cold white light emission at high CCT (8976 K), the LEDs prepared using YMAS:xCe^{3+},yMn^{2+} samples realize warm white light emission with a satisfactory CCT ($\sim$4000 K). The simple synthetic method, effective color point tuning and good stability make YMAS:xCe^{3+},yMn^{2+} an attractive candidate phosphor for warm white LED lighting. This work not only serves as the case for altering the physicochemical properties of the materials with a co-doping strategy and energy transfer process, but also reveals the potential application of YMAS:Ce^{3+},Mn^{2+} in warm white LED lighting.

Conflicts of interest

There are no conflicts to declare.

Acknowledgements

References

1 S. Pimputkar, J. S. Speck, S. P. DenBaars and S. Nakamura, *Nat. Photonics*, 2009, **3**, 179–181.

2 P. Pust, P. J. Schmidt and W. Schnick, *Nat. Mater.*, 2015, **14**, 454–458.

3 E. F. Schubert and J. K. Kim, *Science*, 2005, **308**, 1274–1278.

4 Z. G. Xia and A. Meijerink, *Chem. Soc. Rev.*, 2017, **46**, 275–299.

5 X. D. Chen, X. Zhang and J. T. Du, *Build. Environ.*, 2019, **153**, 168–185.

6 J. A. Lai, Z. W. Long, J. B. Qiu, D. C. Zhou, J. H. Zhou, C. C. Zhu, S. H. Hu, K. Zhang and Q. Wang, *J. Am. Ceram. Soc.*, 2020, **103**, 335–345.

7 K. C. H. J. Smolders and Y. A. W. de Kort, *J. Environ. Psychol.*, 2017, **50**, 80–93.

8 Z. G. Xia and Q. L. Liu, *Prog. Mater. Sci.*, 2016, **84**, 59–117.

9 G. Ao, Y. R. Tang, X. Z. Yi, Y. N. Tian, J. Chen, D. M. Hao, Y. D. Lin and S. M. Zhou, *J. Alloys. Compd.*, 2019, **798**, 695–699.

10 H. Chen, H. Lin, J. Xu, B. Wang, Z. B. Lin, J. C. Zhou and Y. S. Wang, *J. Mater. Chem. C*, 2015, **3**, 8080–8089.

11 Y. C. Jia, Y. J. Huang, Y. H. Zheng, N. Guo, H. Qiao, Q. Zhao, W. Z. Lv and H. P. You, *J. Mater. Chem.*, 2012, **22**, 15146–15152.

12 M. Cui, J. D. Wang, M. M. Shang, J. H. Li, Q. Wei, P. P. Dang, H. S. Jang and J. Lin, *J. Mater. Chem. C*, 2019, **7**, 3644–3655.

13 Y. B. Chen, J. Wang, M. L. Gong, Q. Su and J. X. Shi, *Chem. Lett.*, 2007, **36**, 760–761.

14 H. P. Ji, L. Wang, Y. J. Cho, N. Hirosaki, M. S. Molokeev, Z. G. Xia, Z. H. Huang and R. J. Xie, *J. Mater. Chem. C*, 2016, **4**, 9872–9878.

15 M. M. Shang, J. Fan, H. Z. Lian, Y. Zhang, D. L. Geng and J. Lin, *Inorg. Chem.*, 2014, **53**, 7748–7755.

16 H. S. Jang, W. Bin Im, D. C. Lee, D. Y. Jeon and S. S. Kim, *J. Lumin.*, 2007, **126**, 371–377.

17 H. Y. Sun, X. Zhang and Z. H. Bai, *J. Rare Earths*, 2013, **31**, 231–234.

18 X. T. Zhang, Z. C. An, R. J. Dong, Y. H. Song, K. Y. Zheng, Y. Sheng, S. Zhan and H. F. Zou, *ACS Sustainable Chem. Eng.*, 2019, **7**, 10724–10733.

19 X. T. Zhang, T. Z. Shen, D. X. Kan, D. Zhang, R. J. Dong, Z. C. An, Y. H. Song, K. Y. Zheng, Y. Sheng, Z. Shi and H. F. Zou, *Inorg. Chem.*, 2020, **59**, 9927–9937.

20 Z. C. An, W. Liu, Y. H. Song, X. T. Zhang, R. J. Dong, X. Q. Zhou, K. Y. Zheng, Y. Sheng, Z. Shi and H. F. Zou, *J. Mater. Chem. C*, 2019, **7**, 6978–6985.

21 D. X. Kan, D. S. Wang, X. L. Zhang, R. Q. Lian, J. Xu, G. Chen and Y. J. Wei, *J. Mater. Chem. A*, 2020, **8**, 3097–3108.

22 G. Sun and P. Sautet, *J. Chem. Theory Comput.*, 2019, **15**, 5614–5627.

23 H. M. Chen, L. W. Wu, F. Bo, J. K. Jian, L. Wu, H. W. Zhang, L. R. Zheng, Y. F. Kong, Y. Zhang and J. J. Xu, *J. Mater. Chem. C*, 2019, **7**, 7096–7103.

24 Z. F. Pan, J. C. Chen, H. Q. Wu and W. Q. Li, *Opt. Mater.*, 2017, **72**, 257–264.

25 L. T. Lin, L. X. Ning, R. F. Zhou, C. Y. Jiang, M. Y. Peng, Y. C. Huang, J. Chen, Y. Huang, Y. Tao and H. B. Liang, *Inorg. Chem.*, 2018, **57**, 7090–7096.

26 Z. F. Pan, Y. Xu, Q. S. Hu, W. Q. Li, H. Zhou and Y. F. Zheng, *RSC Adv.*, 2015, **5**, 9489–9496.

27 V. Bachmann, C. Ronda and A. Meijerink, *Chem. Mater.*, 2009, **21**, 2077–2084.

28 T. Senden, R. J. A. van Dijk-Moes and A. Meijerink, *Light: Sci. Appl.*, 2018, **7**, 8.

29 N. P. Holzapfel, J. D. Majher, T. A. Strom, C. E. Moore and P. M. Woodward, *Chem. Mater.*, 2020, **32**, 3510–3516.

30 X. Chen, F. Z. Lv, P. G. Li and Y. H. Zhang, *Opt. Mater.*, 2016, **54**, 276–281.

31 J. Y. Si, L. Wang, L. H. Liu, W. Yi, G. M. Cai, T. Takeda, S. Funahashi, N. Hirosaki and R. J. Xie, *J. Mater. Chem. C*, 2019, **7**, 733–742.

32 C. H. Huang and T. M. Chen, *J. Mater. Chem. C*, 2011, **115**, 2349–2355.

33 R. J. Dong, H. F. Zou, X. T. Zhang, Z. C. An, X. Q. Zhou, K. Y. Zheng, Y. Sheng, Z. Shi and Y. H. Song, *J. Am. Ceram. Soc.*, 2019, **102**, 5284–5294.

34 Z. C. An, H. F. Zou, C. Y. Xu, X. T. Zhang, R. J. Dong, Y. Sheng, K. Y. Zheng, X. Q. Zhou and Y. H. Song, *ACS Sustainable Chem. Eng.*, 2019, **7**, 3154–3163.

35 Y. Xiao, Z. D. Hao, L. L. Zhang, W. G. Xiao, D. Wu, X. Zhang, G. H. Pan, Y. S. Luo and J. H. Zhang, *Inorg. Chem.*, 2017, **56**, 4538–4544.

36 Q. Liu, J. Guo, M. H. Fan, Q. Zhang, S. Liu, K. L. Wong, Z. Y. Liu and B. Wei, *J. Mater. Chem. C*, 2020, **8**, 2117–2122.

37 G. C. Pan, X. Bai, W. Xu, X. Chen, D. L. Zhou, J. Y. Zhu, H. Shao, Y. Zhai, B. Dong, L. Xu and H. W. Song, *ACS Appl. Mater. Interfaces*, 2018, **10**, 39040–39048.

38 J. R. Ling, Y. F. Zhou, W. T. Xu, H. Lin, S. Lu, B. Wang and K. Wang, *J. Adv. Ceram.*, 2020, **9**, 45–54.

39 Q. Bao, Z. J. Wang, J. Sun, Z. P. Wang, X. Y. Meng, K. L. Qiu, Y. Chen, Z. P. Yang and P. L. Li, *Dalton Trans.*, 2018, **47**, 13913–13925.

40 M. Zhao, H. X. Liao, L. X. Ning, Q. Y. Zhang, Q. L. Liu and Z. G. Xia, *Adv. Mater.*, 2018, **30**, 1802489.

41 J. J. Jia, Y. C. Qiang, J. F. Xu, M. Z. Liang, W. Wang, F. L. Yang, J. Cui, Q. Dong and X. Y. Ye, *J. Am. Ceram. Soc.*, 2020, **103**, 5111–5119.